A COMBINED EULERIAN—LAGRANGIAN THREE-DIMENSIONAL FINITE-ELEMENT ANALYSIS OF EDGE-ROLLING

H.J. HUISMAN* and J. HUETINK

Production Division, Department of Mechanical Engineering, Twente University of Technology, P.O. Box 217, 7500 AE Enschede (The Netherlands)

Industrial summary

After edge-rolling (heavy width-reduction), the cross-section of a continuously-cast steel slab may be non-rectangular, whereas what is desired is that it should be exactly rectangular. The deformed shape results in an increased number of heavy width- and thickness-reductions having to be imposed on the slab. Since edge-rolling is clearly a three-dimensional forming process, use of plane-strain analysis would be insufficient: a three-dimensional finite-element formulation, based on elastic—plastic material behaviour, has therefore been developed. This three-dimensional formulation has been incorporated into the existing special purpose FEM programme DIEKA, developed at Twente University of Technology by one of the present authors. The former two-dimensional programme DIEKA has already been successfully applied to plane-strain processes such as the cold rolling of strip-material, and axi-symmetric processes such as wire drawing.

Using the extended three-dimensional programme, calculations have been made in order to investigate the influence of roller-radii on the resulting cross-section of the slab after a width reduction. Experiments for verification and small-scale simulation of the real production process have been carried out using plasticine as a model material.

Notation

$a_{ii} = a_{11} + a_{22} + a_{33}$	(Einstein convention, subscripts only)
$b_{i,j} = \dfrac{\partial b_i}{\partial x_j}$	(partial derivative)
$[B]$	matrix of derivatives of nodal interpolation functions
d_{ij}	rate of deformation tensor
E	Young's modulus
f	body-force vector per unit volume
F	nodal-points load vector of complete body
G	shear modulus
$[K]$	stiffness matrix of complete body
L^k	interpolation function associated with the kth nodal point of an element

*Presently at Marc Analysis, Zoetermeer, The Netherlands.

N	number of nodes per element
r,s,t	natural coordinates of isoparametric elements
s_{ij}	deviatoric-stress tensor
t	time
T	force vector on body surface
x	global-coordinates vector
u	displacement vector
v	velocity vector
W	work, power
δ	variational operator
δ_{ij}	Kronecker's delta; $i{=}j$: $\delta_{ij} = 1$, $i{\neq}j$: $\delta_{ij} = 0$
Δ	increment
$\tilde{\epsilon}^{\mathrm{p}}$	equivalent plastic-strain
μ	coefficient of sliding friction
ν	Poisson's ratio
σ	stress component
σ_{v}	yield stress
σ_{ij}	stress tensor
$\tilde{\sigma}$	equivalent, Von Mises stress
ω_{ij}	vorticity tensor
$\dot{G} = \dfrac{\partial G}{\partial t} + v_i \dfrac{\partial G}{\partial x_i}$	(material rate of change)
$\overset{\nabla}{\sigma}_{ij} = \dot{\sigma}_{ij} - \omega_{ik}\sigma_{kj} - \omega_{jk}\sigma_{ik}$	(Jaumann rate of change)

Basic equations

A forming process can be described in terms of the applied stresses, strains and strain-rates and the (current) geometry of the workpiece. Once the stresses are known, the forces that act on the workpiece/tool can be calculated, together with the power needed to carry out the forming process. The stresses have to satisfy the mechanical equilibrium

$$\sigma_{ij,j} + f_i = 0 \qquad (1)$$

where $\sigma_{ij,j}$ stands for the divergence of the symmetric stress tensor and vector f_i contains the body-forces per unit volume.

The rates of deformation can be obtained by decomposing the partial derivatives of the velocity vector into a symmetric and an asymmetric part

$$\left.\begin{aligned} v_{i,j} &= d_{ij} + \omega_{ij} \\[4pt] d_{ij} &= \tfrac{1}{2}(v_{i,j} + v_{j,i}) \\[4pt] \omega_{ij} &= \tfrac{1}{2}(v_{i,j} - v_{j,i}) \end{aligned}\right\} \qquad (2)$$

where tensor d_{ij} is known as the rate of deformation tensor, and ω_{ij} (not contributing to the deformation) is called the vorticity tensor.

The equations that define the relationships between stresses and strains are called constitutive equations: in the present case, as will be seen later, these appear to be constitutive rate equations. Firstly, the conditions that must be satisfied in order to achieve plastic deformation have to be specified. Assuming isotropic material behaviour, the Von Mises yield criterion [1] can be applied. Using the following notation for the deviatoric stress tensor

$$s_{ij} = \sigma_{ij} - \frac{1}{3} \sigma_{kk} \delta_{ij} \tag{3}$$

the criterion states that plastic deformation occurs if

$$s_{ij} s_{ij} = 2k^2 \tag{4}$$

in which $k = \sigma_v / \sqrt{3}$, where σ_v represents the current yield stress in a tensile test. Equation (4) is often written as

$$\frac{2}{3} \tilde{\sigma}^2 = 2k^2 \tag{5}$$

where $\tilde{\sigma}$ is known as the equivalent Von Mises stress.

According to the results of experiment, the yield stress is assumed to be a function of the equivalent plastic strain ($\tilde{\epsilon}^p$), the strain-hardening parameter that takes into account the plastic-deformation history of a material particle. Hence (in plastic deformation)

$$\tilde{\sigma} = \tilde{\sigma}(\tilde{\epsilon}^p) \tag{6}$$

By decomposing the rate of deformation tensor into an elastic and a plastic part according to

$$d_{ij} = d_{ij}^e + d_{ij}^p \tag{7}$$

the equivalent plastic strain can be expressed in d_{ij}^p as

$$\tilde{\epsilon}^p = \int_0^t \left(\frac{2}{3} d_{ij}^p d_{ij}^p \right)^{\frac{1}{2}} \mathrm{d}t \tag{8}$$

At $t = 0$ the material is, according to eqn. (8), free of plastic strain and is called 'dead soft'.

The constitutive equations applicable in the elastic region consist of a modified formulation of Hooke's law [2], which for small elastic strains can be expressed as [3, 4]

$$\overset{\triangledown}{\sigma}_{ij} = E_{ijkl} d_{kl}^e \tag{9}$$

where $\overset{\triangledown}{\sigma}_{ij}$ is the Jaumann rate of change of the stress tensor and

$$E_{ijkl} = \frac{E}{2(1 + \nu)} \left(\delta_{ik}\delta_{jl} + \delta_{il}\delta_{jk} + \frac{2\nu}{1 - 2\nu} \delta_{ij}\delta_{kl} \right) \tag{10}$$

The relationship between the plastic part of the rate of deformation tensor and the deviatoric stress tensor follows from the Drucker postulation [5]

$$d_{ij}^{\mathrm{p}} = \lambda s_{ij} \tag{11}$$

By using this relationship, the Von Mises yield condition as given earlier, and eqns. (5) and (7), the following elastic—plastic constitutive rate equations can be derived [4, 6]

$$\overset{\triangledown}{\sigma}_{ij} = D_{ijkl} d_{kl} \tag{12}$$

with

$$D_{ijkl} = E_{ijkl} - (3G^2 \ s_{ij}s_{kl}) \left\{ \left(G + \frac{1}{3}\frac{d\tilde{\sigma}}{d\tilde{\epsilon}^{\mathrm{p}}} \right) \tilde{\sigma}^2 \right\}^{-1} \tag{13}$$

Note: these equations describe the behaviour of an isotropic material under isothermal conditions.

Finite-element formulation

The previously described equations have to be suitably elaborated to be solved with the finite-element method: the solution will, in general, be an approximation. Starting from mechanical equilibrium, eqn. (1) will be

$$\int_V (\sigma_{ij,j} + f_i)\delta v_i \mathrm{d}V = 0 \qquad \forall\, \delta v_i \tag{14}$$

This formulation is known as the weak formulation of the equilibrium. The vector δv, containing the components δv_i, is called the virtual velocity vector. It is possible to lower the order of the highest derivative of σ_{ij} in eqn. (14). To achieve this, the Gauss divergence theorem can be applied

$$\delta W = \int_V \sigma_{ij}\delta d_{ij}\mathrm{d}V - \int_V f_i\delta v_i\mathrm{d}V - \int_S T_i\delta v_i\mathrm{d}S = 0 \qquad \forall\, \delta v_i \tag{15}$$

which is known as the equation of the virtual power. T_i are components of the stress vector, acting on the surface part $\mathrm{d}S$ of the material surface S, bounding the volume V. Equation (15) holds for every type of material.

Elastic—plastic material behaviour is described using eqn. (12). Under the given definition of the Jaumann rate of change, this equation results in

$$\dot{\sigma}_{ij} = D_{ijkl}d_{kl} + \omega_{ik}\sigma_{kj} + \omega_{jk}\sigma_{ik} \tag{16}$$

Note that this expression for $\dot{\sigma}_{ij}$ (the material rate of change) cannot be substituted directly into the equation for the virtual power: it is necessary to include also the material rate of change of δW in eqn. (15). Straightforward manipulation and substitution of the expression of $\dot{\sigma}_{ij}$ given by eqn. (16) leads to [7]

$$\delta \dot{W} = \int\limits_V (D_{ijkl}d_{kl}\delta d_{ij} - 2\sigma_{kj}d_{ik}\delta d_{ij} + \sigma_{ij}v_{k,j}\delta v_{k,i} + \sigma_{ij}\delta d_{ij}v_{k,k})\,\mathrm{d}V$$

$$(17)$$

$$- \int\limits_V (\dot{F}_i\delta v_i + F_i\delta v_i v_{k,k})\mathrm{d}V - \int\limits_S \left(\dot{T}_i\delta v_i + T_i\delta v_i \frac{\mathrm{d}\dot{S}}{\mathrm{d}S}\right)\mathrm{d}S = 0 \qquad \forall\,\delta v ,$$

where $\mathrm{d}\dot{S}/\mathrm{d}S$ denotes the specific change of the outer surface. This equation can be regarded as the governing equation to be solved for the independent field variables; in the case of the FEM programme DIEKA these are velocities.

In the finite-element formulation, the volume of the material subjected to deformation is divided into parts, in this case into three-dimensional elements. In the FEM programme DIEKA these are hexahedron elements with 8 or 20 nodes, as shown in Fig. 1. These elements can be characterized by the fact that the shape (global coordinates), or geometry, is described in the same way as the independent field variables (velocities)

$$x_i = \sum_{k=1}^{N} L^k(r,s,t)x_i^k \qquad (i = 1, 2, 3)$$

$$v_i = \sum_{k=1}^{N} L^k(r,s,t)v_i^k \qquad \text{and} \qquad \delta v_i = \sum_{k=1}^{N} L^k(r,s,t)\delta v_i^k$$

$$(18)$$

These elements are therefore called isoparametric [8]. L^k are interpolation functions, the values of which depend on the natural, intrinsic coordinates r, s and t [9]. N is equal to the number of nodes per element (8 or 20). x_i^k and v_i^k are the nodal-point global coordinates and velocities respectively (superscripts refer to nodal-point numbers).
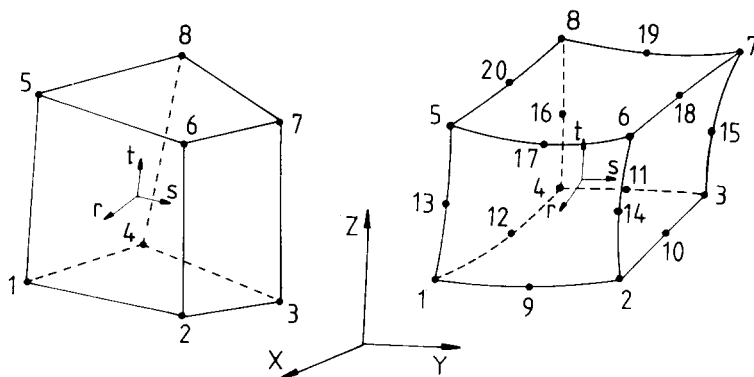

Fig. 1. Three-dimensional hexahedron elements: (a) bi-linear element; (b) quadratic element.

The partial derivatives of the global velocities follow from eqn. (18)

$$v_{i,j} = \sum_{k=1}^{N} L_{,j}^{k}(r,s,t)v_i^k \qquad \text{with} \qquad L_{,j}^{k} = \frac{\partial L^k}{\partial x_j} \tag{19}$$

This notation for $v_{i,j}$ allows expression of the rate of deformation tensor (d_{ij}) in nodal-point velocities.

After arranging the partial derivatives of the interpolation functions into the so-called B-matrix, the following relationship between d (vector containing the six independent components of the symmetric tensor d_{ij}) and v_e (vector containing the nodal-point velocities) is obtained

$$d = [B] \cdot v_e \tag{20}$$

A similar expression can be derived to express the vorticity tensor ω_{ij} in the nodal-point velocities.

Starting from a known state, it is possible to substitute eqns. (18), (19) and (20) into eqn. (17). The (weaker) condition that the resulting expression is equal to zero with respect to all possible virtual nodal velocities δv^k is then applied. The boundary conditions are enforced to find the following set of linear equations

$$[K] \cdot v = \dot{F} \tag{21}$$

The matrix $[K]$ is called the stiffness matrix; the vector v contains all degrees of freedom of the system (nodal-point velocities). The vector $\dot{F}$ is called the load-rate vector. The completion of eqn. (21) will not be discussed in detail, as it is the same as the usual finite-element discretization in linear problems [9, 10]. It should be noted just that integration of the integrals in eqn. (17) is performed numerically [8, 9].

From the solution of eqn. (21), the nodal-point velocities, (v_i^k), will result. If these are assumed to persist for a time increment Δt, it is possible to calculate approximately the change of the stress-tensor components in the integration points from eqns. (16) and (18), by

$$\Delta \sigma_{ij} = \Delta t(D_{ijkl}d_{kl} + \omega_{ik}\sigma_{kj} + \omega_{jk}\sigma_{ik}) \qquad (= \dot{\sigma}_{ij}\Delta t) \tag{22}$$

It can be noted from eqn. (13) that the change of the stress tensor, as shown by eqn. (22), depends implicitly on the current stress-state.

In the case of an Updated Lagrangian approach [6], the nodal points are coupled with the material points. In this case the new stresses in the integration points are found by adding $\Delta \sigma_{ij}$ (from eqn. 22) to the corresponding stress components just before the time increment. If an Eulerian reference frame is designated, the nodal points are not coupled with specific material particles throughout the simulation process: the material flows through the elements. Hence it will be necessary to alter eqn. (22) in order to find the new stresses in integration points of the fixed reference mesh. The incremental change of the stress tensor is then given by the following approximation

$$\Delta\sigma_{ij} = (\overset{\circ}{\sigma}_{ij} - v_l\sigma_{ij,l})\Delta t \tag{23}$$

so that instead of the material rate of change, the time derivative $(\partial/\partial t)$ is used to calculate the stress changes. The algorithm to calculate $\sigma_{ij,l}$ will be discussed in detail later.

A Lagrangian approach is applicable to transient problems, whereas an Eulerian formulation is often used in steady-state problems. A combination of these two approaches consists of coupling the nodal-point displacements to some extent to the displacements of the material points that coincide with the nodal points just before a time increment (see Fig. 2). This combined Eulerian—Updated Lagrangian finite-element formulation can be applied to steady-state, large-deformation processes where not all material surface-movements are imposed by the tool geometry or symmetry conditions. Often, an Updated Lagrangian approach is not suitable because of the large number of elements that have to be used to find the steady-state solution of the forming process. Further, it takes considerable effort to adapt the continuously changing boundary conditions. A purely Eulerian formulation cannot take into account a free-surface motion since the reference mesh is fixed in space. The combined Eulerian—Updated Lagrangian finite-element formulation is therefore applied to the edge-rolling process.
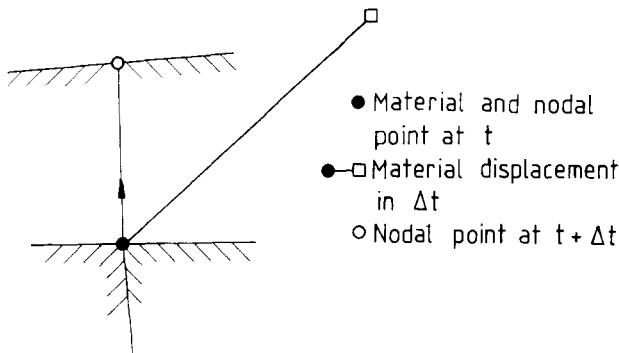

Fig. 2. Uncoupled material and nodal-point displacements.

There are several options for altering the positions of the nodal points in actual computations with the three-dimensional sub-frame of the FEM programme DIEKA. Once these new positions are known, the programme can calculate the new stresses and strains in the integration points (their positions are related to the element shape and the integration equation [8, 11]), after a time increment Δt.

Some of the options in altering the nodal-point coordinates are outlined below.

(i) One coordinate remains unchanged. The programme user can apply this useful option to the coordinate in the dominating velocity direction. See Fig. 3a.
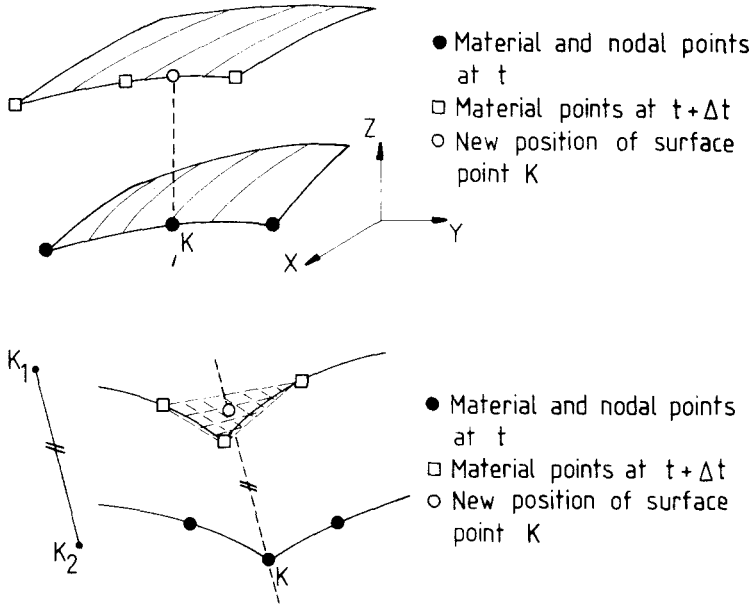
340

Fig. 3. Two options to alter the position of a surface node: (a) one coordinate remains unchanged; (b) new position drawn from the intersection K_1K_2 and the locally approximated surface in K.

(ii) An external surface (or an internal surface that forms the boundary between two different materials), can be locally approximated, using the position of three points. The intersection of the surface drawn from the material displacement after a time-increment Δt, and for a given direction, will show the new position of the nodal (surface) point. In Fig. 3b the points K_1 and K_2 are used to indicate the direction of displacement. Instead of using two points, the displacement direction can be determined by a vector normal to the surface at $t = 0$.

Once the position of every nodal point connected to an element is known, the new locations of the integration points are also determined (the intrinsic, natural coordinates remain unchanged, as they depend only on the numerical-integration equation used).

The algorithm applied to calculate the new stresses in the integration points is outlined below. To illustrate the algorithm, a two-dimensional, quadrilateral element with four nodes and one integration point is shown in Fig. 4. A stress-tensor component $\overset{1}{\sigma}$ in the material point that coincides with the new integration point after a time increment Δt follows from

$$\overset{1}{\sigma} = \overset{0}{\sigma}_m + \int_{t=0}^{\Delta t} \dot{\sigma}_m \, dt \tag{24}$$

where the stress component at $t = 0$ in the material point $(\overset{0}{\sigma}_m)$ can be written as (Taylor-series in the integration point)

$$\overset{0}{\sigma}_m = \overset{0}{\sigma} + \overset{0}{\sigma}_{,l}\Delta u_l + O(\Delta u)^2 \tag{25}$$

$\overset{0}{\sigma}$ denotes the value of the stress in the integration point at $t = 0$ and Δu shows the difference in location between the integration point and the material point at $t = 0$ (see Fig. 4).
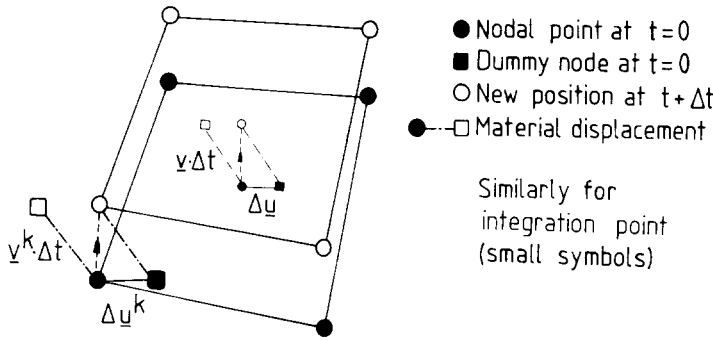

Fig. 4. Situations of an integration point in a quadrilateral element.

The second term on the right-hand side of eqn. (25) can be computed by defining an additional stress-field (σ') using the stress values in N dummy nodes (the same number of nodes as in the element-type used). Firstly, the stress values in the relevant dummy points have to be specified. The stress values in these nodes (σ'^k) depend on the values in the actual nodal points (σ^k) and the distance between the dummy nodes and actual nodal points.

A stress-tensor component in an actual nodal point is computed as an average taken from all elements coupled to the nodal point. For each element, the nodal-point value is calculated from the stress values in the integration points of the elements by extrapolation, and by using a least-squares algorithm [12] for the case of 27 Gaussian integration points. From Δu^k (see Fig. 4), showing the distance between the dummy nodes and actual nodal points resulting from the solution vector v (eqn. 21), the change in the intrinsic coordinates (dr^n, ds^n, dt^n) of nodal point n can be obtained. The intrinsic coordinates of dummy node n are then written as $(r^n + dr^n, ..)$. The stresses in the dummy nodes can now be expressed as

$$\overset{0n}{\sigma'} = \sum_{k=1}^{N} L^k(r^n + dr^n, s^n + ds^n, t^n + dt^n)\overset{0k}{\sigma}, n = 1,2, .. N \tag{26}$$

Hence the additional stress-field becomes

$$\overset{0}{\sigma}{}'(r,s,t) = \sum_{k=1}^{N} L^k(r,s,t)\overset{0k}{\dot{\sigma}{}'} \tag{27}$$

Using eqn. (27) the second term in the Taylor-seres (eqn. 25) can, after some manipulation, be written as

$$\overset{0}{\sigma}{}_{,l}\Delta u_l \approx \sum_{k=1}^{N} L^k(r,s,t)\,(\overset{0k}{\sigma}{}' - \overset{0k}{\sigma}) \tag{28}$$

where the intrinsic, natural coordinates of the integration point are used.

The new stress in the integration point can now be calculated (from eqns. 24, 25 and 26) as

$$\overset{1}{\sigma} = \overset{0}{\sigma} + \sum_{k=1}^{N} L^k(r,s,t)\,(\overset{0k}{\sigma}{}' - \overset{0k}{\sigma}) + \int_{t=0}^{\Delta t} \dot{\sigma}_{\mathrm{m}}\,\mathrm{d}t \tag{29}$$

The incremental change in the stress given by the integral is calculated using eqns. (13), (20), (21) and (22). Thus, the displacement after a time increment ($v\cdot\Delta t$ in Fig. 4) is assumed to be the same for the material point flowing towards the integration point, as for the integration point itself!

Application to edge-rolling

At the rougher in a hot-strip mill, slabs of steel (temperature $\sim 1200°$C) are rolled not only by horizontal flat-rolls but also by vertical edge-rolls. The purpose of width reduction by edge rolling is twofold: the removal of the oxide-skin from the slab surface and the forming of bulk into a particular width to secure the desired final strip-width with minimum mill margin. One of the important technical problems concerning edge-rolling is controlling the cross-sectional shape of the material formed: after edge-rolling this shape may be non-rectangular. Sometimes, because of its similarity in appearance, this deformed shape is termed 'dog-bone'.

To develop an optimal rolling scheme it is necessary to determine the dependency of slab cross-sections on the various process parameters (rolling-speed, reduction, roll-sizes, etc.). In this paper the influence of roll-radii on the cross-sectional slab shape in edge-rolling is examined (see Fig. 5). Investigations have been carried out in the past by others, either experimental [13, 14] or numerical [15, 16]: the latter, however, are based on rigid—plastic material behaviour.

To examine the influence of roll-radii, two edge-rolling processes have been analyzed with the FEM programme DIEKA, the processes differing only in the roll-radii: calculations have been carried out for a small roll-radius (R = 50 mm) and a large roll-radius (R = 700 mm). Plasticine is used as the forming material, both in the analyses and in the experiments: this material is used frequently to simulate the actual hot-rolling process

in scaled-down experiments at room temperature. The process conditions are outlined in Table 1; data of the forming material are given in Table 2.

Starting from the symmetrical nature of the forming process (symmetry around the slab-centre along the slab-width and the slab-thickness), it is possible to minimize calculational effort: only one quarter of the slab is discretized into elements and appropriate boundary conditions are applied to simulate the actual symmetry. The elements used are 20-node hexahedron elements (see Fig. 1), with 14-point numerical integration as given by Irons [11].
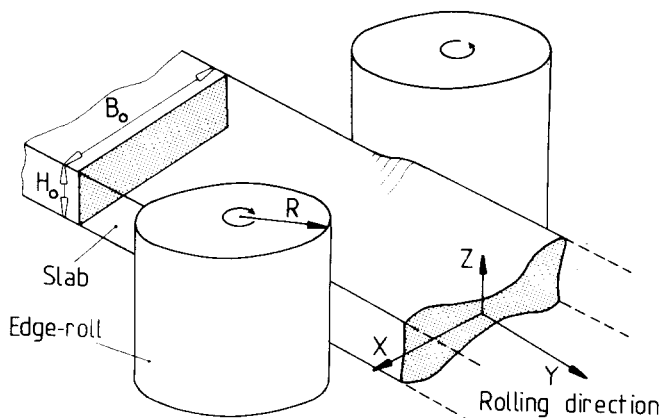
Fig. 5. Schematic diagram of the edge-rolling process.

TABLE 1

Numerical and experimental process conditions for single-pass edge-rolling

Width of slab B_0 (mm)	140
Thickness of slab H_0 (mm)	22.5
Edging draft (mm)	8
Roll-radii R (mm)	50 or 700
Rolling temperature (°C)	20
Rolled material	Plasticine
Lubrication	None

TABLE 2

Mechanical properties of plasticine (at 20°C)

Colour	Yellow/green
Young's modulus E (N/mm²)	10
Poisson's ratio ν	0.4
Constant yield stress assumed σ_{v} (N/mm²)	0.12
Coefficient of sliding friction at the plasticine/roll interface, μ	1.2

In the analysis the combined Eulerian—Lagrangian finite-element formulation is used: the positions of the nodal points at the upper free mesh-surface are adapted continuously in the thickness-direction, and nodal points on the side of the slab (after the roll-gap exit) are connected to the material displacement in the transverse direction. In the *initial* finite-element mesh discretization, the nodal points at the upper surface are positioned at half the slab-thickness ($Z = 11.25$). Since friction along the slab/roll interface is large, sticking is assumed (therefore the roll surface and nodes show no relative motion along this surface). The numerical results are first discussed, and are afterwards compared with the results of the experiments.

The finite-element mesh for the case of $R = 50$ mm is shown in Fig. 6. The total number of elements is 32 and the mesh is refined in the contact zone because of the deformation expected near to the slab-edges. Most of the following illustrations are cross-sections in the transverse direction at $Z = 0$. The mean total displacement in the dominating velocity direction has been 34 mm (0.4 mm/increment), i.e., about 1.5 times the contact-arc length.
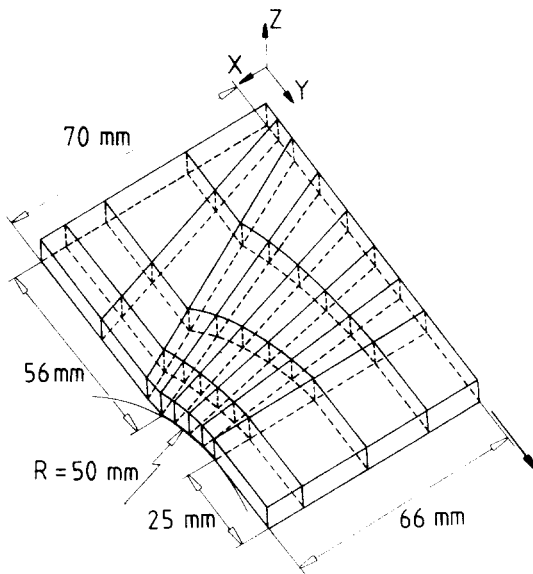
Fig. 6. FEM mesh for the case of $R = 50$ mm (initial geometry).

The location of the plastically deforming region in the slab can be drawn from the distribution of the Von Mises stress (see Fig. 7). At a yield stress of 0.12 N/mm², plastic deformation already occurs before the gap entrance. Moreover, plastic deformation spreads from the slab-edge (at entry), over about a quarter of the slab-width (towards the roll-gap exit).
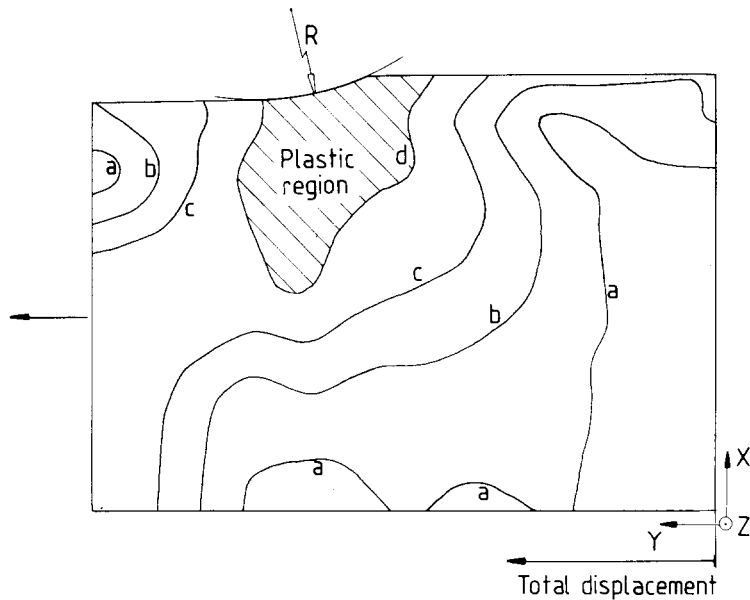
Fig. 7. Distribution of the Von Mises stress in the slab at $Z = 0$. Contour values (N/mm^2): $a = 0.040$; $b = 0.067$; $c = 0.093$; $d = 0.120$.

The transverse stress (σ_{11}) as drawn in Fig. 8, shows a minimum negative value (pressure), in the contact zone. A small negative level at the slab centre $(X = 0)$ combined with the roll pressure provides the necessary mechanical equilibrium in the transverse direction.
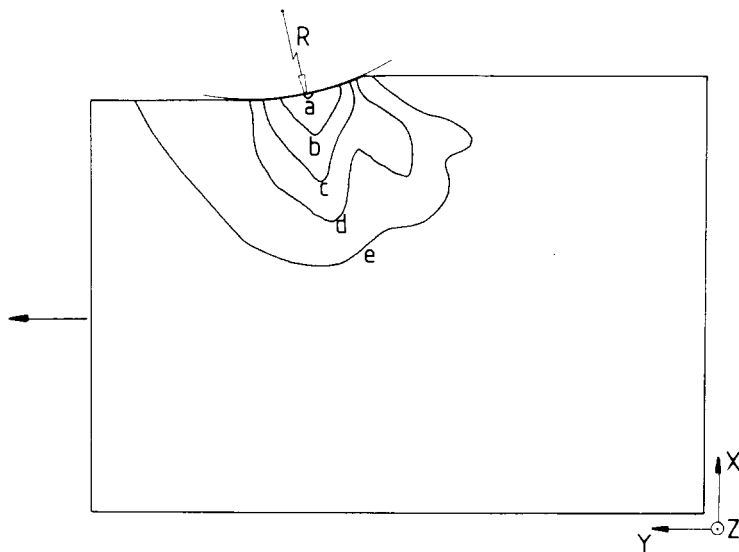

Fig. 8. Transverse stress in the slab at $Z = 0$. Contour value (N/mm^2): $a = -0.514$; $b = -0.390$; $c = -0.275$; $d = -0.155$; $e = -0.036$.

The radial stress normal to the roll/slab interface at $Z = 0$ and the shear stress in the interface are shown in Figs. 9 and 10. The minimum value in the pressure curve is found half-way along the distance between the gap-entry and the gap-exit. The levels at entry and exit differ from zero because of the algorithm applied to calculate the nodal-point stresses (extrapolation errors), and because of discretizing of the material into elements. The distribution of the shear-stress curve is in agreement with the assumed sticking-condition. It can be shown that this curve is quite different from the shear-
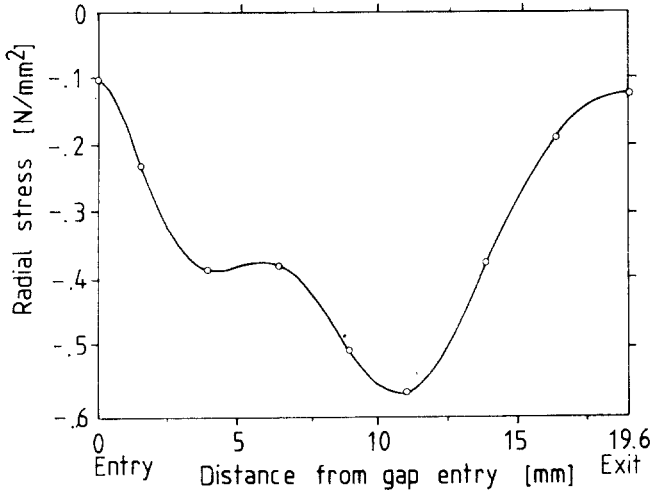
Fig. 9. Radial stress normal to the roll/slab interface at $Z = 0$.
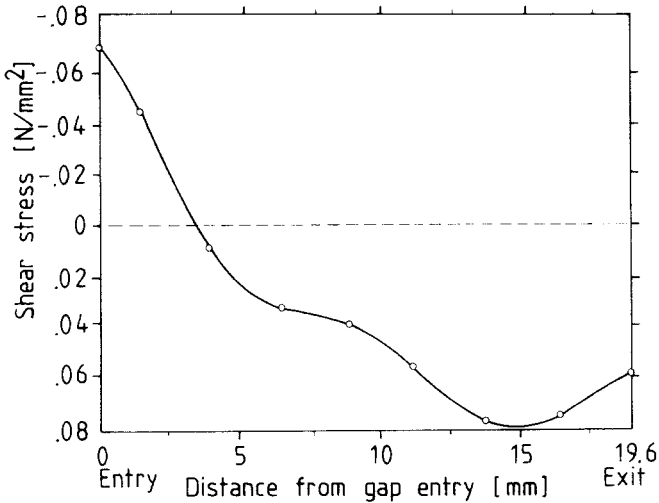
Fig. 10. Shear stress in the rolling direction at the roll/slab interface.

stress curve found in the rolling of thin sheet: in the latter case a neutral point N is assumed in the roll/sheet interface. From entry towards N the rolls are moving faster than the forming material; from N towards exit, the rolls are moving more slowly than the material. The friction force between the rolls and the forming material must therefore be directed towards the neutral point, the direction of the shear stress changing also [17].

The distribution of the equivalent plastic strain (Fig. 11) shows the plastic deformation to be concentrated in the slab edges (as already concluded from Fig. 7). The distance between zero level a (see Fig. 11) and maximum level g is equal to the total displacement in the rolling direction.

The velocity field (in the rolling direction) is shown in Fig. 12. At the down-stream side can be noted an increase from the slab-edge towards the slab-centre, whereas the field should be homogeneous in the material that has already been rolled. More elements, covering extra down-stream material, would be appropriate to simulate the steady-state nature of the process. Slab in the up-stream side of the roll-gap is simulated correctly, as shown by the uniformly distributed velocity field.

The distribution of the velocities in the transverse- and thickness-directions, in three cross-sections of the slab, are drawn in Fig. 13. From Figs. 13a and 13b the conclusion can be drawn that the slab material near to the centre does not move significantly in either of the two directions; at entrance or half-way along the contact-arc. The completion of the dog-bone near to the edge of the slab is clearly visible.
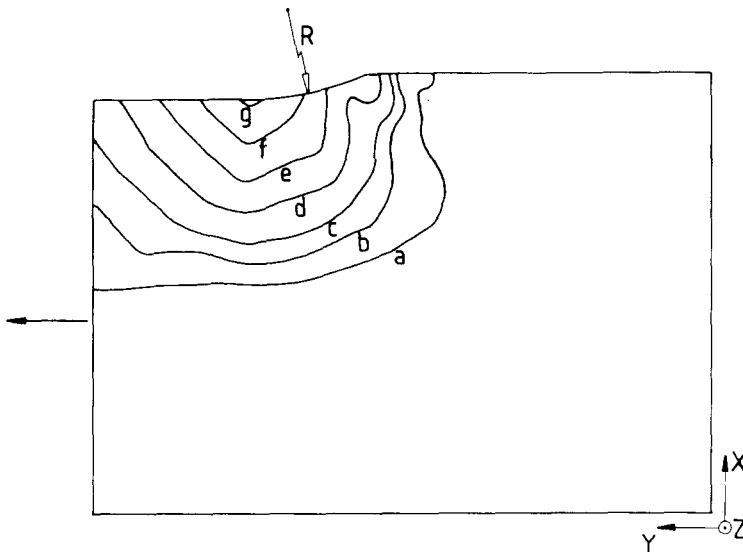

Fig. 11. Distribution of the equivalent plastic strain in the slab at $Z = 0$. Contour values (%): $a = 0.0$; $b = 6.3$; $c = 12.6$; $d = 22.1$; $e = 31.6$; $f = 41.4$; $g = 50.5$.
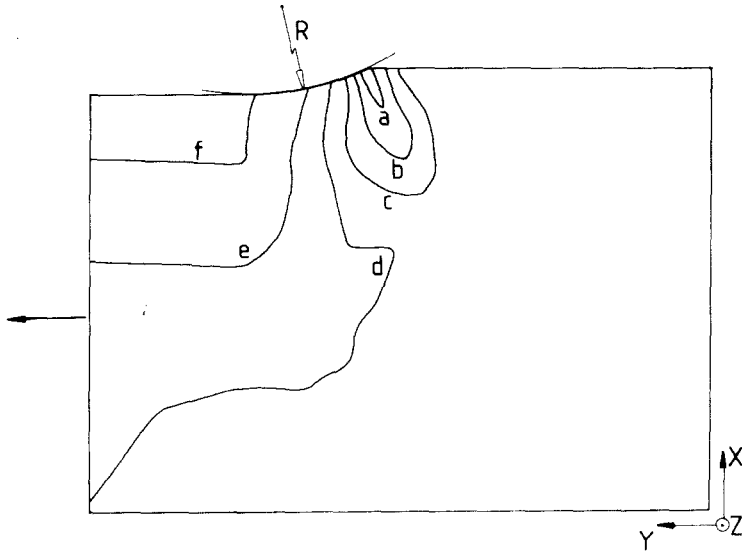
Fig. 12. Velocity field in rolling direction at $Z = 0$. Contour values (%): $a = 36.0$; $b = 37.0$; $c = 37.7$; $d = 38.5$; $e = 39.0$; $f = 40.0$.
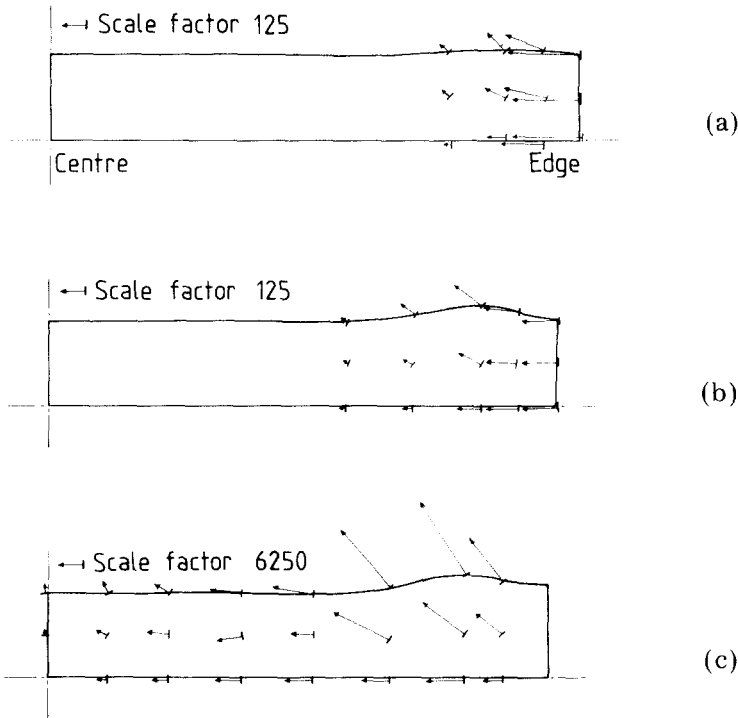

Fig. 13. Velocities in three cross-sections of the slab during rolling; (a) at entrance; (b) half-way across the contact zone; (c) at the roll-gap exit.

The final shape of the slab cross-section is shown in Fig. 14. The shaded area represents the FEM mesh cross-section at the roll-gap exit. Other quadrants have been drawn by using the symmetry of the process. The dog-bone peak is located at 11 mm from the side of the slab; the height calculated is 27.314 mm (2 × 13.657).

Calculations have also been carried out for the case of R = 700 mm (a magnification of the roll-radius by a factor of fourteen). The finite-element mesh as shown in Fig. 15 consists of only 10 elements because the deformation is assumed to be quite homogeneous. The contact zone is described
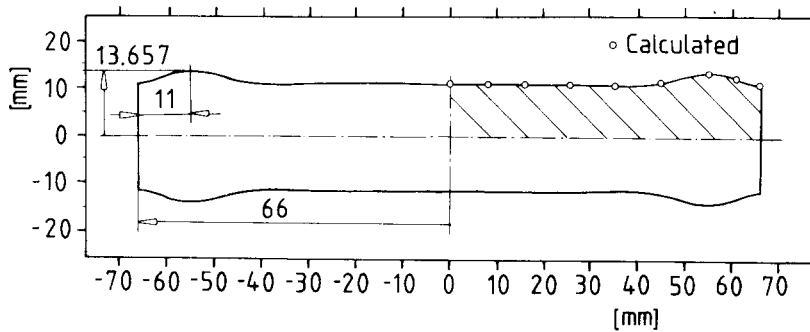
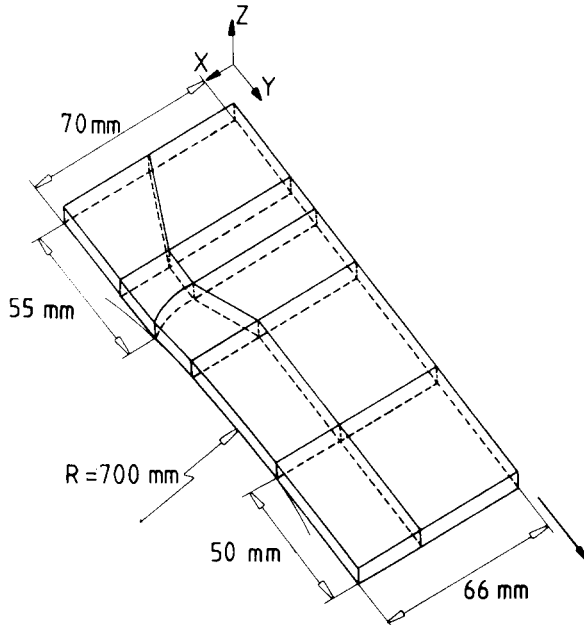Fig. 14. Sectional shape of the dog-bone, as calculated.

Fig. 15. FEM mesh for the case of R = 700 mm (initial geometry).

by two elements. The distribution of the Von Mises stress is shown in Fig. 16. The total displacement has been 117 mm (1.3 mm/increment), again 1.5-times the contact-arc length. Plastic deformation occurs before the entrance, and material is being deformed plastically over the complete slab-width, unlike the situation where $R = 50$ mm.
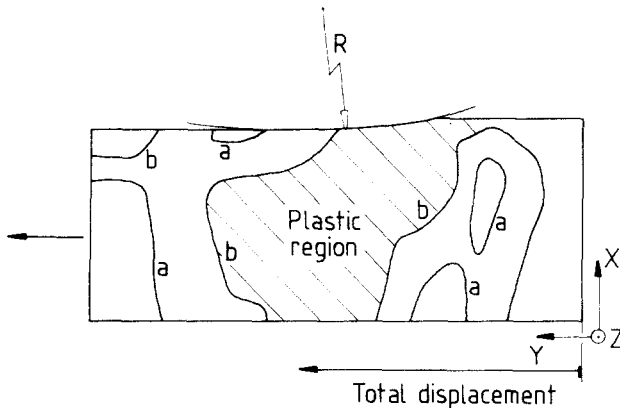

Fig. 16. Distribution of the Von Mises stress in the slab at $Z = 0$. Contour values (N/mm^2); $a = 0.093$; $b = 0.120$.

The distribution of velocities in the transverse- and thickness-directions is drawn in Fig. 17. The dominance of the transverse velocity (Figs. 17a and 17b) — not only near to the slab-edge but also near to the centre — is quite obvious. The direction of the transverse velocity reverses in the roll-gap exit (Fig. 17c): attention should be paid to the relatively large scale-factor of Fig. 17c compared to that of Figs. 17a and 17b.

The final cross-section (Fig. 18) shows no strict dog-bone shape; the edge-rolling pass has caused the slab thickness to increase from the centre towards the edge. The maximum height calculated is 24.092 mm (2 × 12.046).

Experiments have been carried out to verify the numerical results: for the case of $R = 50$ mm the rolling load was measured. The process conditions are listed in Table 1. In the experiments the length of the slabs was equal to 430 mm, being made relatively great compared with thickness and width, in order to be able to simulate the steady-state nature of the numerically-analyzed processes.

The experimental equipment for the case of $R = 700$ mm, as developed by the Royal Dutch Hoogovens Group B.V., consists of two circular shaped segments. A pendular mill design had been chosen for practical reasons: the dimensions of an actual mill would be extremely large if two complete rolls were to be used. The resulting experimental cross-sectional shape for the case of $R = 50$ mm is shown in Fig. 19: the positions of the nodal points on the upper surface are drawn in the same plot for comparison
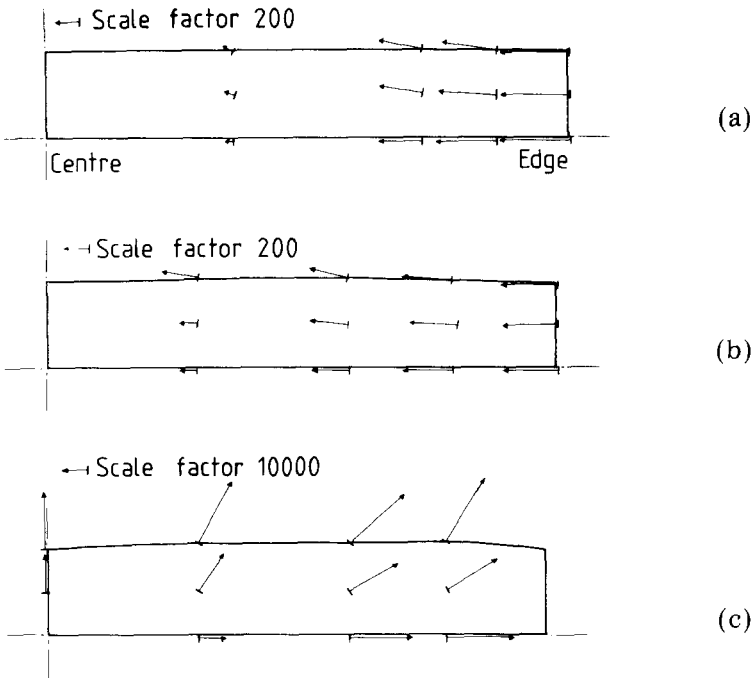
Fig. 17. Velocities in three cross-sections of the slab during rolling. (a) at entrance; (b) half-way across the contact zone; (c) at the roll-gap exit.
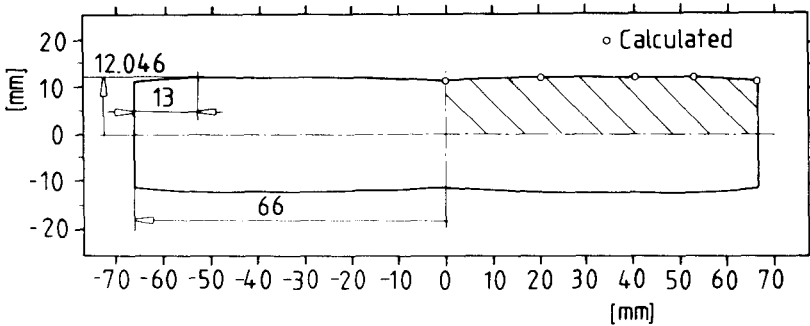

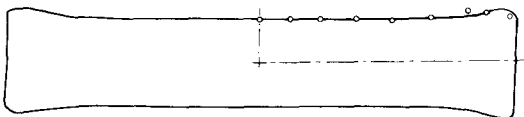Fig. 18. Sectional shape of the slab after rolling, as calculated.

Fig. 19. Comparison of sectional shapes obtained by experiment with those obtained by numerical analysis, for the case of R = 50 mm.

with the numerical results. In the experiments, the sectional shape for the case of $R = 700$ mm appeared to be quite similar to the numerically obtained cross-section (see Fig. 18).

Experimental and numerical results are listed in Table 3. The smaller roll-radii ($R = 50$ mm) produce uneven deformation with a large dog-bone peak: to achieve slab-lengthening by edge-rolling, roll-radii of 700 mm are preferable therefore to $R = 50$ mm. However, rolling load and rolling torque, (hence also mill load), are greater for the case of $R = 700$ mm.

TABLE 3

Experimental and numerical (in parentheses) results of the single-pass edge-rolling process

Subject	$R = 50$ mm	$R = 700$ mm
Maximum dog-bone height	27.4 (27.314)	23.9 (24.092)
Rolling load (N)	95 (106)	— (291)
Rolling torque (Nm)	— (1.4)	— (11.8)

Conclusions

(1) The combined three-dimensional Eulerian—Updated Lagrangian finite-element formulation developed has been successfully applied to the edge-rolling process, the numerical results being in reasonable agreement with those of the experiments carried out.

(2) Both numerical analyses and experiment show small roll-radii ($R = 50$ mm) to be less efficient than large roll-radii ($R = 700$ mm) in effecting width-reduction of the plasticine model-material employed.

(3) The analysis of slab rolling has been demonstrated to be a feasible application of the FEM programme DIEKA: developments of the latter in the near future concern extensions of the programme to achieve the ability to simulate the flattening of the dog-bone.

Acknowledgement

References

1 A. Mendelson, Plasticity, Theory and Application, Collier-MacMillan, London, 1968.
2 S.P. Timoshenko and J.M. Gere, Mechanics of Materials, Van Nostrand Reinhold, London, 1973.
3 W. Prager, Introduction to Mechanics of Continua, Dover, New York, NY, 1961.

4 J.F. Besseling, Trends in Solid Mechanics, Proc. Symp. 65th Birthday of W.T. Koiter, Delft University Press, Sijthoff & Noordhoff, 1979, pp. 53—78.

5 D.C. Drucker, Some implications of work hardening and ideal plasticity, Quart. Appl. Math., 7 (1950) 411—418.

6 H.D. Hibbitt, P.V. Marcal and J.R. Rice, A finite element formulation for large strain and large displacement, Int. J. Solids Struc., 6 (1970) 1069—1086.

7 J. Huetink, Analysis of metal forming processes based on a combined Eulerian—Lagrangian finite element formulation, Proc. Int. Conf. on Numerical Methods in Industrial Forming Processes, Pineridge Press, Swansea, 1982, pp. 501—509.

8 O.C. Zienkiewicz, The Finite Element Method in Engineering Science, McGraw-Hill, London, 1971.

9 S.S. Rao, The Finite Element Method in Engineering, Pergamon Press, Oxford, 1982.

10 C.A. Brebbia and J.J. Connor, Fundamentals of Finite Element Techniques for Structural Engineers, Butterworth, London, 1973.

11 B.M. Irons, Quadrature rules for brick based elements. Int. J. Num. Meth. Eng., 3 (1971) 293—294.

12 E. Hinton and J.S. Campbell, Local and global smoothing of discontinuous finite element functions using a least-square method, Int. J. Num. Meth. Eng., 8 (1974) 461—480.

13 H. Hirano, H. Ibata, H. Kitawani and I. Kokubo, Width necking at the rougher in a hot-strip mill, J. Mech. Work. Technol., 7 (1983) 367—383.

14 M. Takeuchi, O. Hirata, M. Hoshiya, T. Kikuma, K. Watanabe and S. Sadahiro, Heavy width reduction rolling of slabs, Nippon Steel Technical Report, 21 (1983) 235—246.

15 K. Mori and K. Osakada, Simulation of three-dimensional rolling by the rigid—plastic finite element method, Proc. Int. Conf. on Numerical Methods in Industrial Forming Processes, Pineridge Press, Swansea, 1982, pp. 747—756.

16 H. Takuda, K. Mori, N. Hatta and J. Kokado, Experiment and finite element analysis of hot rolling of slab in width reduction with flat roll, J. Jap. Soc. Tech. Plasticity, 23 (1982) 1103—1108.

17 J.N. Harris, Mechanical Working of Metals, Theory and Practice, Pergamon, Oxford, 1983.